

Voxel-wise uncertainty in CT substitute derived from MRI

Adam Johansson, Mikael Karlsson, Jun Yu, Thomas Asklund, and Tufve Nyholm

Citation: *Medical Physics* **39**, 3283 (2012); doi: 10.1118/1.4711807

View online: <http://dx.doi.org/10.1118/1.4711807>

View Table of Contents: <http://scitation.aip.org/content/aapm/journal/medphys/39/6?ver=pdfcov>

Published by the [American Association of Physicists in Medicine](#)

Articles you may be interested in

Description and assessment of a registration-based approach to include bones for attenuation correction of whole-body PET/MRI

Med. Phys. **40**, 082509 (2013); 10.1118/1.4816301

Comparison of image registration based measures of regional lung ventilation from dynamic spiral CT with Xe-CT

Med. Phys. **39**, 5084 (2012); 10.1118/1.4736808

Concurrent segmentation of the prostate on MRI and CT via linked statistical shape models for radiotherapy planning

Med. Phys. **39**, 2214 (2012); 10.1118/1.3696376

CT substitute derived from MRI sequences with ultrashort echo time

Med. Phys. **38**, 2708 (2011); 10.1118/1.3578928

CT and MRI derived source localization error in a custom prostate phantom using automated image coregistration

Med. Phys. **28**, 2280 (2001); 10.1118/1.1406525

NEW!

Quality Reports™

Evaluate, Score, and Benchmark Your Plan Quality





SUN NUCLEAR
corporation

At a Glance!

- ✓ Metrics you want
- ✓ Information you need
- ✓ Less time, less effort
- ✓ Works with all TPS and modalities



Watch Now! ▶

Voxel-wise uncertainty in CT substitute derived from MRI

Adam Johansson^{a)} and Mikael Karlsson

Department of Radiation Sciences, Umeå University, Umeå, SE-901 87 Sweden

Jun Yu

Centre of Biostochastics, Swedish University of Agricultural Sciences, Umeå, SE-901 87 Sweden

Thomas Asklund and Tufve Nyholm

Department of Radiation Sciences, Umeå University, Umeå, SE-901 87 Sweden

(Received 13 February 2012; revised 13 April 2012; accepted for publication 20 April 2012; published 22 May 2012)

Purpose: In an earlier work, we demonstrated that substitutes for CT images can be derived from MR images using ultrashort echo time (UTE) sequences, conventional T2 weighted sequences, and Gaussian mixture regression (GMR). In this study, we extend this work by analyzing the uncertainties associated with the GMR model and the information contributions from the individual imaging sequences.

Methods: An analytical expression for the voxel-wise conditional expected absolute deviation (EAD) in substitute CT (s-CT) images was derived. The expression depends only on MR images and can thus be calculated along with each s-CT image. The uncertainty measure was evaluated by comparing the EAD to the true mean absolute prediction deviation (MAPD) between the s-CT and CT images for 14 patients. Further, the influence of the different MR images included in the GMR model on the generated s-CTs was investigated by removing one or more images and evaluating the MAPD for a spectrum of predicted radiological densities.

Results: The largest EAD was predicted at air-soft tissue and bone-soft tissue interfaces. The EAD agreed with the MAPD in both these regions and in regions with lower EADs, such as the brain. Two of the MR images included in the GMR model were found to be mutually redundant for the purpose of s-CT generation.

Conclusions: The presented uncertainty estimation method accurately predicts the voxel-wise MAPD in s-CT images. Also, the non-UTE sequence previously used in the model was found to be redundant. © 2012 American Association of Physicists in Medicine.

[<http://dx.doi.org/10.1118/1.4711807>]

Key words: magnetic resonance imaging, computed tomography substitute, ultrashort echo time, quality assurance, Gaussian mixture, dose calculation, attenuation correction

I. INTRODUCTION

The possibility of deriving CT equivalent information from MR images has attracted a lot of attention in recent years. Derivation of electron density information from MR data is a prerequisite for an MR based radiotherapy workflow¹ and for an effective use of a combined PET/MR scanner² without the need to integrate a rotating radiation source into the already limited space of the PET/MR gantry. It is not possible to directly measure electron density with an MR scanner as can be done with CT scanners due to the fundamentally different physical processes involved in generating the measured signals, i.e., nuclear magnetic resonance versus x-rays. It is also nontrivial to derive an indirect relation between the electron density and MR signal in human tissue. This stems from the similar appearance of air and cortical bone in images from conventional MRI sequences, a similarity caused by the short T2* of bone.^{3,4} By contrast, the electron densities of air and bone are very different. However, a number of different indirect methods have been described and evaluated in the literature. Each method is associated with uncertainties that can affect either the geometrical position

of a specific voxel or the intensity of the voxel, or both. These uncertainties can typically be quantified on a population level, but as the uncertainties can be highly individual, there is a need to quantify the uncertainties for the individual patient or even on a voxel level if a reliable uncertainty estimate is to be obtained. Reliable uncertainty estimates of the electron density could then be used to estimate uncertainties in standardized uptake values (SUV) for PET/MR or absorbed dose for a MRI based radiotherapy work-flow.

The effect of errors in attenuation maps on reconstructed PET images has been investigated using simulations of a human torso phantom.⁵ The simulations showed that replacing the attenuation coefficient of cortical bone with that of soft tissues or the attenuation coefficient of lung tissue with that of air gave errors up to 17% and 45%, respectively. A study of MRI based attenuation correction in the head region indicated that radiotracer concentrations could be underestimated or overestimated by more than 20% if cortical bone or internal air cavities were not correctly accounted for. For radiotherapy, the differences in dose for plans based on homogeneous and CT-based electron densities are in the range of 0.9%–2.5%.^{6–8} For brain treatments, the range is 1%–1.5%.^{9,10}

Two approaches for estimating the electron density from MR images dominate the literature: atlas^{11–13} and voxel based.^{14–16} Atlas based methods use reference sets of CT data for typical patients and then registers these sets with MR images of a new patient, either directly through CT–MR registration or indirectly through MR–MR registration when MR images are available within the reference set. Atlas methods have proven useful in the head region where problems with non-rigid registrations are relatively small. Schreibmann *et al.* have investigated non-rigid registration between CT atlas and MR images for 17 clinical brain cancer cases. In general, the results were very accurate. However, for individual patients, geometrical errors of more than 3 mm were observed for up to 27% of the bony structures.¹¹ Atlas based methods are, in general, considered robust in terms of average pixel intensities but suffer from geometrical uncertainties, especially in body regions other than the head. Also, they provide no mechanism to account for interpatient variability of bone or lung tissues. Hofmann *et al.* have described a promising method to account for local registration errors using a second step of pattern recognition to fine tune the voxel characterization.¹² This method could in principle provide not only the most likely pixel value for a derived pseudo-CT but also the uncertainty in this estimation. The authors, however, do not take this step.

By contrast, voxel based methods aim at characterization of individual voxels based on the imaged MR properties. Characterization can either be segmentation into different tissue classes¹⁷ followed by bulk density assignments, or a direct prediction of the Hounsfield unit (HU) for each voxel. Voxel based methods do not rely on interpatient image registration as atlas based methods do and are thus less prone to geometrical errors. Two publications from 2010 presented segmentation methods based on MR sequences with ultra-short echo times (UTE).^{14,15} The results showed that the UTE approach enables a separation of bone and air, which is problematic with traditional MR techniques. However, the segmentation step limits the potential. We raise three objections to the use of a segmentation step when estimating a CT equivalent image from MR data. First, methods classifying voxels into bone, air, and soft tissue cannot handle partial volume effects and, therefore, rely on high spatial resolution, which can be time consuming. Second, segmentation into a single bone class does not reflect the wide range of different bone densities that can be found in, for example, the head and neck region¹⁸ or between different patients. Third, the segmentation step makes it difficult to estimate the HU uncertainty for individual voxels since tissues with different uncertainties are placed in the same group, e.g., soft tissues situated close or far from to air or bone interfaces.¹⁹

Previously, we reported on a method for generating a substitute CT image (s-CT) from MR images.¹⁹ Due to differences between the CT and MR imaging modalities, the s-CT cannot be expected to exactly match an actual CT image. This work analyzes the inherent uncertainties in the previously described s-CT concept. Also, for clinical application an MRI based radiotherapy work-flow and for attenuation correction in PET/MR the scanning time required for an s-CT

should be minimized. Therefore, possible exclusion of individual MRI sequences from the s-CT method is investigated.

In the theory section, we derived an expression for estimating the HU uncertainty in an s-CT on a voxel level as well as tools for evaluating this expression. We continue by describing materials and methods for evaluation both the accuracy of the uncertainty estimation expression as well as the contribution from individual MR images to the accuracy of the s-CT image. The results of application of these methods are then presented and their implications discussed.

II. THEORY

In a prior publication, we described a method for representing the combined information in a set of registered MR and CT images as a Gaussian mixture regression (GMR) model.¹⁹ The GMR model was applied to an MR data set for a new patient to estimate the CT information for that patient on a voxel by voxel level. The method was evaluated for an MR data set of UTE images that provided separation between air, soft tissue, and bone, combined with a high resolution T2 weighted sequence and provided seemingly accurate results. In the GMR model, for each voxel, the intensities from the CT and MR images are treated as an observation from a Gaussian mixture distribution. From the images of one or more patients, the distribution parameters can be estimated using expectation maximization (EM). Subsequently, a regression function that maps MR intensities to CT Hounsfield unit values can be derived from the Gaussian mixture. Below, derivation of the inherent uncertainties in HU estimation in the GMR model is undertaken. Stochastic variables and their observations are denoted by upper case and lower case letters, respectively.

Let $G(\mathbf{z}; \boldsymbol{\mu}, \Sigma)$ denote a multivariate Gaussian distribution for a stochastic variable \mathbf{Z} such that

$$G(\mathbf{z}; \boldsymbol{\mu}, \Sigma) = \frac{1}{(2\pi)^{k/2} |\Sigma|^{1/2}} \exp\left(-\frac{1}{2}(\mathbf{z} - \boldsymbol{\mu})^T \Sigma^{-1} (\mathbf{z} - \boldsymbol{\mu})\right), \quad (1)$$

where k , $\boldsymbol{\mu}$, and Σ is the number of elements in \mathbf{z} , the mean value vector and the covariance matrix, respectively. With \mathbf{Z} partitioned as

$$\mathbf{Z} = \begin{pmatrix} \mathbf{X} \\ \mathbf{Y} \end{pmatrix} \quad (2)$$

and $\boldsymbol{\mu}$, and Σ similarly partitioned as

$$\boldsymbol{\mu} = \begin{pmatrix} \boldsymbol{\mu}_X \\ \boldsymbol{\mu}_Y \end{pmatrix}, \quad (3)$$

$$\Sigma = \begin{pmatrix} \Sigma_{XX} & \Sigma_{XY} \\ \Sigma_{YX} & \Sigma_{YY} \end{pmatrix}, \quad (4)$$

it can be shown²⁰ that the conditional distribution of $\mathbf{Y}|\mathbf{X}$ is Gaussian and can be written as

$$f_{Y|X}(y|\mathbf{x}) = \frac{G(\mathbf{z}; \boldsymbol{\mu}, \boldsymbol{\Sigma})}{G(\mathbf{x}; \boldsymbol{\mu}_X, \boldsymbol{\Sigma}_{XX})} = G(y; \tilde{\boldsymbol{\mu}}, \tilde{\boldsymbol{\Sigma}}) \quad (5)$$

with

$$\tilde{\boldsymbol{\mu}}(\mathbf{x}) = \boldsymbol{\mu}_Y + \boldsymbol{\Sigma}_{XY} \boldsymbol{\Sigma}_{XX}^{-1} (\mathbf{x} - \boldsymbol{\mu}_X), \quad (6)$$

$$\tilde{\boldsymbol{\Sigma}} = \boldsymbol{\Sigma}_{YY} - \boldsymbol{\Sigma}_{XY}^T \boldsymbol{\Sigma}_{XX}^{-1} \boldsymbol{\Sigma}_{XY}. \quad (7)$$

For a multivariate Gaussian mixture regression model, the distribution of voxel intensities, $f_Z(\mathbf{z})$, in a multidimensional intensity space is described by a weighted sum of N multivariate Gaussian distributions

$$f_Z^{\text{mix}}(\mathbf{z}) = \sum_{i=1}^N a_i G(\mathbf{z}; \boldsymbol{\mu}_i, \boldsymbol{\Sigma}_i), \quad (8)$$

where \mathbf{Z} denotes the intensities for the different image types and the parameters describing the distribution are the mixing proportions a_i , mean values $\boldsymbol{\mu}_i$, and covariance matrices $\boldsymbol{\Sigma}_i$. Let the intensity vector be partitioned as in Eq. (2) with \mathbf{Y} representing the Hounsfield value in the CT and \mathbf{X} the intensities in the MR images and let each of $\boldsymbol{\mu}_i$ and $\boldsymbol{\Sigma}_i$ be partitioned as in Eqs. (3) and (4). The conditional distribution of $\mathbf{Y}|\mathbf{X}$ is then²¹

$$f_{Y|X}^{\text{mix}}(y|\mathbf{x}) = \sum_{i=1}^N w_i(\mathbf{x}) G(y; \tilde{\boldsymbol{\mu}}_i(\mathbf{x}), \tilde{\boldsymbol{\Sigma}}_i) \quad (9)$$

with

$$w_i(\mathbf{x}) = \frac{a_i G(\mathbf{x}; \boldsymbol{\mu}_{i,X}, \boldsymbol{\Sigma}_{i,XX})}{\sum_{j=1}^N a_j G(\mathbf{x}; \boldsymbol{\mu}_{j,X}, \boldsymbol{\Sigma}_{j,XX})}. \quad (10)$$

The conditional expectation for the Hounsfield value given a set of observed MR intensities is then

$$\mathbf{m}(\mathbf{x}) = E(\mathbf{Y}|\mathbf{X} = \mathbf{x}) = \sum_{i=1}^N w_i(\mathbf{x}) \tilde{\boldsymbol{\mu}}_i(\mathbf{x}). \quad (11)$$

This expression was used to generate the s-CT. The conditional variance of the Hounsfield value for a voxel with observed MR intensities is similarly given by

$$\begin{aligned} v(\mathbf{x}) &= \text{Var}(\mathbf{Y}|\mathbf{X} = \mathbf{x}) \\ &= \sum_{i=1}^N w_i(\mathbf{x}) (\tilde{\boldsymbol{\Sigma}}_i + \tilde{\boldsymbol{\mu}}_i(\mathbf{x}) \tilde{\boldsymbol{\mu}}_i^T(\mathbf{x})) - \mathbf{m}(\mathbf{x}) \mathbf{m}^T(\mathbf{x}). \end{aligned} \quad (12)$$

For the general GMR case where \mathbf{Y} is a vector, $v(\mathbf{x})$ is a matrix describing the expected uncertainty in the predicted value of \mathbf{Y} . For the subject at hand, $\mathbf{Y} = Y$ is a scalar, and thus, $v(\mathbf{x})$ is also scalar and is equivalent to the expected squared deviation between Y and the scalar $\mathbf{m}(\mathbf{x}) = m(\mathbf{x})$. To evaluate whether $v(\mathbf{x})$ is a good estimate of uncertainty, it may be compared to the mean squared prediction deviation (MSPD) defined as

$$\text{MSPD} = \frac{1}{n} \sum_{j=1}^n (y_j - m(\mathbf{x}_j))^2, \quad (13)$$

where n is the number of voxels in the region for which the MSPD is evaluated, y_j is the observed Hounsfield value, and $m(\mathbf{x}_j)$ is the predicted Hounsfield value for voxel j . Another prediction error measure, which is less sensitive to outliers and therefore more robust, is the mean absolute prediction deviation (MAPD) given by

$$\text{MAPD} = \frac{1}{n} \sum_{j=1}^n |y_j - m(\mathbf{x}_j)|. \quad (14)$$

Similarly to the expected squared deviation in Eq. (12), we may calculate the expected absolute deviation (EAD) from the conditional expectation, also known as the first absolute central moment. The EAD is given by (see the Appendix for derivation)

$$\begin{aligned} d(\mathbf{x}) &= \sum_{i=1}^N w_i(\mathbf{x}) \left(\sqrt{\frac{2\tilde{\sigma}_i^2}{\pi}} \exp\left(-\frac{(m(\mathbf{x}) - \tilde{\mu}_i(\mathbf{x}))^2}{2\tilde{\sigma}_i^2}\right) \right. \\ &\quad \left. + (m(\mathbf{x}) - \tilde{\mu}_i(\mathbf{x})) \text{erf}\left(\frac{m(\mathbf{x}) - \tilde{\mu}_i(\mathbf{x})}{\sqrt{2\tilde{\sigma}_i^2}}\right) \right), \end{aligned} \quad (15)$$

where $\tilde{\mu}_i(\mathbf{x})$ and $\tilde{\sigma}_i^2$ are scalar versions of $\tilde{\boldsymbol{\mu}}_i(\mathbf{x})$ and $\tilde{\boldsymbol{\Sigma}}_i$. For a single Gaussian, the standard deviation is equal to the first absolute central moment times the factor $\sqrt{2/\pi}$. For a Gaussian mixture, this relationship does not hold but is still approximately valid if

$$w_i(\mathbf{x}) \approx 1 \quad (16)$$

for some i , i.e., when \mathbf{x} is close to one of the Gaussians $G(\mathbf{x}; \boldsymbol{\mu}_{i,X}, \boldsymbol{\Sigma}_{i,XX})$ in the Gaussian mixture, as determined by the Mahalanobis distance, but far from all the others. This in combination with the independence of $\tilde{\sigma}_i^2$ on \mathbf{x} causes such voxels to have almost the same $d(\mathbf{x})$.

Finally, in analog with the MSPD and MAPD, and as a measure of bias in the s-CT, we can define the mean prediction deviation (MPD)

$$\text{MPD} = \frac{1}{n} \sum_{j=1}^n (y_j - m(\mathbf{x}_j)). \quad (17)$$

III. MATERIALS AND METHODS

III.A. Image acquisition and preprocessing

Data including CT and MR images of the heads of 14 patients were available for this study. For each patient, five MR images were used: four UTE images with varying echo times and flip angles and one T2 weighted SPACE sequence.^{22,23} The five MR images used to estimate the substitute CT images are listed in Table I. Two dual echo UTE sequences were used, with a 10° and 60° nominal flip angle, respectively. Each UTE sequence generated images for both

TABLE I. Acquisition properties for the images used in s-CT generation.

Sequence type	Echo time, TE (ms)	Repetition time, TR (ms)	Flip angle, α	Scan time	Model			
					a	b	c	d
UTE	0.07	6	10°	3 min	•	•	•	•
UTE	3.76	6	10°		•	•		•
UTE	0.07	6	60°	3 min	•		•	•
UTE	3.76	6	60°		•			•
SPACE	100	1500	150°	5 min	•	•	•	

a 0.07 ms and a 3.76 ms echo. Differences between images from these two echoes indicate the presence of short T2* tissues. Differences between UTE images with the same echo time but different flip angles can be used as an indicator for T1, even for tissues with short T2*. A short T2* is not only found in tissues with a short T2, but also in regions with rapid coherent dephasing, such as air–soft tissue and bone–soft tissue interfaces. Information about T1 can help to distinguishing bone from these interfaces. The last image was selected to identify cerebrospinal fluid as this tissue, due to its long T1, has a weak signal in the UTE images. SPACE is a Siemens 3D TSE sequence with variable flip angle refocusing pulses.

The MR image data set was expanded with high- and low-pass filtered counterparts for each MR image. These images provided additional information such as the proximity to edges and local homogeneity of individual voxels, which can help to predict coherent dephasing and thereby short T2*. Images of the same patient were coregistered to achieve voxel-wise correspondence between the images. A binary mask excluding the air surrounding the head was calculated, and all calculations described below were confined to the data found within this mask.

Additional details concerning image acquisition, filtering, registration, and mask calculation are described in our previous publication.¹⁹

III.B. Evaluation of uncertainty estimation method

To evaluate the accuracy of the voxel-wise uncertainty measure in Eq. (15), the parameters in the GMR model were estimated using expectation maximization algorithm on the data from 13 patients. These parameters were then used with the MR data of the 14th patient to estimate the voxel-wise EAD. The voxels were then binned according to their EAD into intervals 20 HU wide. Finally, Eq. (9) was used to calculate a substitute CT that was compared to the real CT for the 14th patient and the difference was used to calculate the MAPD for each bin. Since all voxels in each bin have the same EAD (within 20 HU) the corresponding MAPD should be close to this EAD if the EAD is a good prediction of the true absolute deviation. Parameter estimation and uncertainty calculations were repeated in a leave-one-out cross-validation procedure with the 14 patients cyclically permuted for each cross-validation fold. Parameter estimation was performed according to our previously described method.¹⁹

For comparison the MAPD that resulted from replacing a CT image with a segmented CT image was also checked for all patients. The CT images were then segmented into three classes: less than –400 HU, between –400 HU and 400 HU and above 400 HU, roughly corresponding to air pockets, soft tissues, and bone. For each class, the voxel values were set to the mean of the corresponding voxels in the CT.

III.C. Evaluation of information content in individual MR images

The impact of each MR image on the s-CT method can be investigated by constructing s-CT images from a subset of the acquired MR images. This is accomplished by repeating the full cross-validation procedure with one or more of the images in Table I and their filtered counterparts eliminated. Three cases aside from the full model were investigated. The images that were excluded were in the first model derived from the UTE sequence with a 60° flip angle, in the second model from the 3.76 ms echoes of both UTE sequences and in the third model from the T2 weighted SPACE sequence. The four models are labeled (a)–(d) in Table I. Exclusion of the different images could lead not only to an increased uncertainty of the predicted s-CT values but also to systematic deviations.

IV. RESULTS

IV.A. Evaluation of uncertainty estimation method

The joint histogram in Fig. 1 illustrates the relationship between the expected HU value from Eq. (11) and the EAD from Eq. (15) for a patient. Figure 1 also shows in what regions four tissue classes appear in the joint histogram. The gentle horizontal lines seen in Fig. 1 correspond to voxels

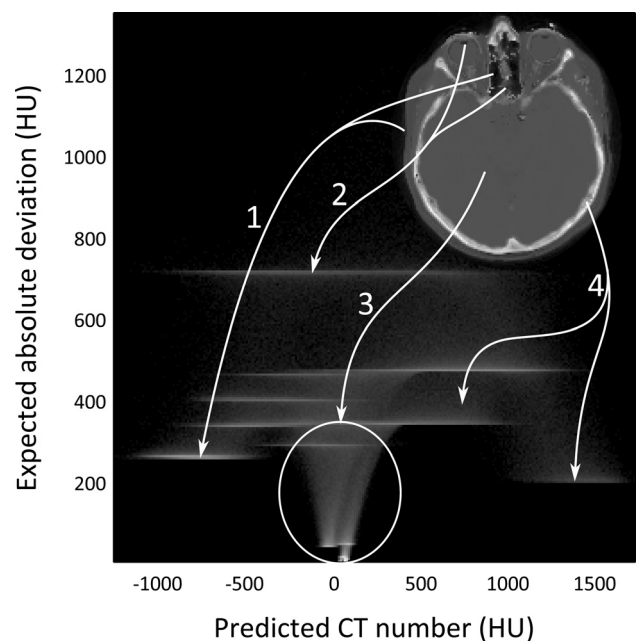


FIG. 1. Joint histogram of the EAD versus the expected HU value the voxels of one patient. Arrows show where four tissue classes appear in the joint histogram. Arrow 1: air; arrow 2: soft tissues with short T2*; arrow 3: soft tissues; arrow 4: bone. The joint histogram is drawn with a logarithmic intensity scale.

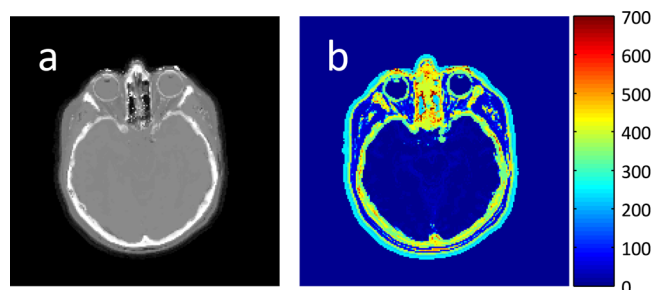


FIG. 2. (a) Sample s-CT for a patient and (b) corresponding EAD for each voxel.

that meet Eq. (16) and points that are positioned in between the lines correspond to voxels that do not.

The EAD is illustrated on a voxel level in Fig. 2. The errors are expected to be large in high and low density regions and at tissue interfaces. The largest uncertainties are estimated for the cornea, where the s-CT method also fails to accurately estimate the HU.

The MAPD between the HU value in the CT and substitute CT calculated from voxels binned according to their EAD is presented in Fig. 3. The relation appears to be approximately linear. The mean cross-validation linear regression coefficient between EAD and the absolute deviation between s-CT and CT for all patients with a forced intercept at the origin was 0.78 with a standard deviation of 0.08.

IV.B. Evaluation of information content in individual MR images

Figure 4 shows the MAPD between the CT and s-CT for all patients as a function of the estimated s-CT value, both for the complete set of MR data and with three different curves representing the use of one UTE flip angle, one UTE echo time and exclusion of the T2 weighted sequence from

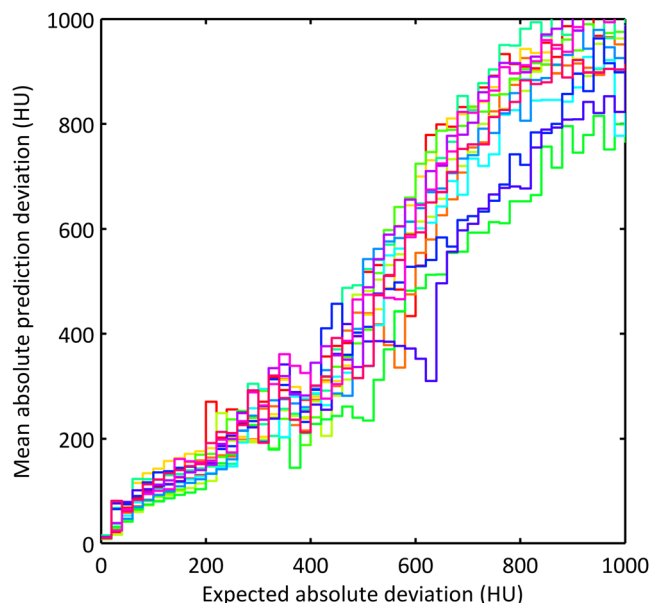


FIG. 3. MAPD versus EAD. Each curve represents one patient and each plateau a 20 HU wide bin in which the absolute prediction deviations were pooled to calculate the MAPD.

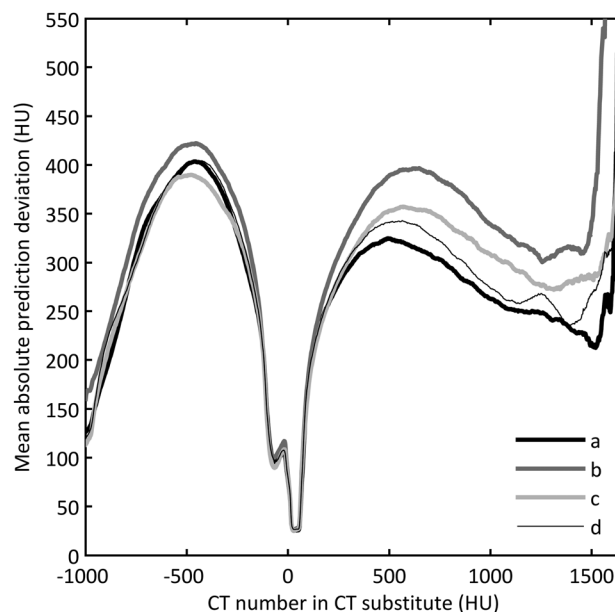


FIG. 4. The MAPD versus s-CT HU values. In the four different scenarios, we used (a) all acquired images, (b) one flip angle (10°), (c) one echo time (0.07 ms), and (d) the all but the T2 weighted images. The MAPD was calculated using a sliding bin 20 HU wide.

the model. The local minima in the MAPD in Fig. 4 for s-CT values around -1000 , 0 , and 1400 HU are paralleled by low values of the EAD in the joint histogram in Fig. 1 for the same s-CT values. The distances from the curve representing the complete model in Fig. 4 to the curves for the reduced models are related to the information loss associated with the corresponding removed images. For example, the removal of the information gained when using two different flip angles affects the s-CT by reducing the quality of the s-CT both in high and low density regions. The MPD, i.e., systematic error or bias, as function of the predicted s-CT values are shown in Fig. 5. Comparing Figs. 4 and 5, it is clear that most of the deviations in the very low density regions are systematic, i.e., the density of air is systematically overestimated by around 100 HU. For the higher densities, the non-systematic errors are dominating. It can also be seen that models built on a single flip angle gave systematic errors for voxels with densities corresponding to mixtures between air and soft tissue, while the complete model tended to provide better results. Removal of the 3.76 ms echoes or the T2 weighted SPACE images led to slightly increased MAPDs across most densities.

For the segmented CT images, the mean MAPD for all patients was 130 HU for air pockets, 60 HU for soft tissues, and 300 HU for bone.

V. DISCUSSION

This study outlines a method for estimation of the voxel-wise uncertainty of the HU estimation in an s-CT derived from MR information. The possibility to derive CT equivalent data from MR information is highly interesting in radiotherapy applications in order to facilitate a straightforward workflow for dose calculations based on MR data.⁶ The s-CT

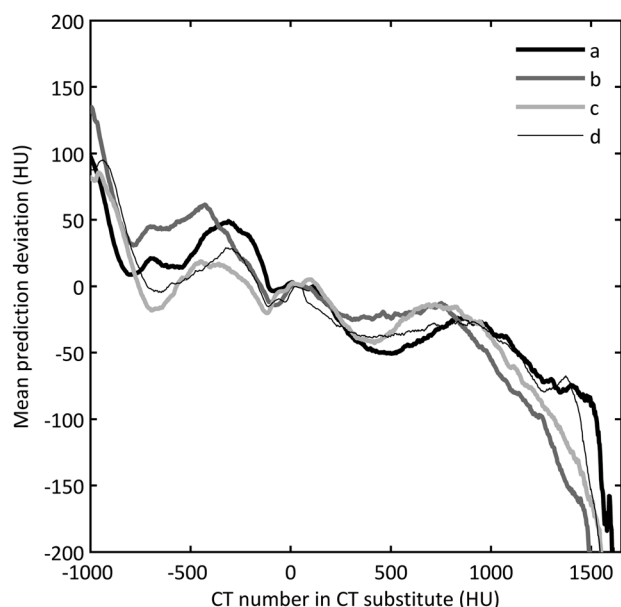


Fig. 5. The MPD between s-CT and CT versus the s-CT HU values. In the four different scenarios, we used (a) all acquired images, (b) one flip angle (10°), (c) one echo time (0.07 ms), and (d) the all but the T2 weighted images. The MPD was calculated using a sliding bin 20 HU wide.

concept also has the potential in a combined PET/MR application to enable attenuation correction based on MR information. In both of these applications, it is of utmost importance to keep the introduced uncertainties under control. This involves not only rigorous quality assurance of the data acquisition for the individual patient but also of the inherent uncertainties introduced by the s-CT method. The uncertainties in the s-CT are as shown in the result section highly dependent on both the tissue and surrounding tissue types. Thus, characterization of the uncertainty on a voxel level is necessary in order to be able to use the uncertainty information. For example, Figs. 1 and 2 show that the s-CT uncertainty in the cornea and in the soft tissue connected to the postnasal sinuses is substantial, while the uncertainties in white and gray matter are very small even though the real electron densities for these volumes are similar. The voxel by voxel representation could make it possible to directly propagate the HU uncertainty to uncertainty in absorbed dose or standardized uptake. Figure 3 shows that the uncertainty prediction method is reasonably accurate. It should be noted that a vast majority of the voxels are associated with estimated uncertainties below 400 HU, while just a very small fraction are associated with uncertainties above 800 HU. Therefore, the left hand side of Fig. 3 is based on a much larger sample than the right hand side. The mean regression coefficient between EAD and the absolute s-CT–CT deviation was only 0.78, which indicates that the EAD overestimates the absolute deviation by 20% on average.

Figures 4 and 5 illustrate the impact of the information content in each of the MR sequences, which was used as input to the GMR model. From Fig. 4, we concluded that the use of UTE sequences with two flip angles substantially increased the quality of the s-CT with a reduction in MAPD of 100 HU (or 25%) for intermediate bone densities. Use of

only one flip angle resulted in larger errors, both at interfaces between air and soft tissue, and in bony parts. Interestingly, the use of only one echo-time in the model (0.07 ms) resulted in less reduction of the s-CT quality. This shows that the $T2^*$ related information acquired with multiple echo-times was, to a large degree, redundant, while the T1 related information from use of two flip angles contributed to a greater extent to the accuracy of the model. Similarly, removal of the SPACE sequence resulted in a small increase of the MAPD. However, if both 3.76 ms echoes and the SPACE sequence were removed, the cerebrospinal fluid was consistently assigned a too low HU value. Systematic errors in s-CT were primarily found at very low and very high predicted HU values, corresponding to air pockets and very dense bone. For dense bone, the systematic errors were paralleled with large MAPD. For all other tissues, the systematic errors were small compared to the MAPD.

The MAPD calculated for all voxels is about 140 HU.¹⁹ However, some sites have larger deviation as seen in Fig. 4, e.g., air–soft tissue interfaces (400 HU) and bone (200–300 HU). Others sites, such as most soft tissues have much smaller errors (around 20 HU). Referring to Fig. 4, it can be noted that the deviations for different radiological densities are equal in magnitude to the deviations between a CT and a segmented CT (air pockets—130 HU, soft tissues—60 HU, and bone—300 HU). Only for air–soft tissue interfaces are the deviations in an s-CT larger. Thus, s-CT images could function in any application where segmented CT images have been shown to work as replacements for CT images. For soft tissues the deviations in an s-CT is smaller than the deviations in a segmented CT. This is due to the high soft-tissue contrast in the MR, and in extension the s-CT, images. This feature of the s-CT could allow it to function as a replacement for CT images for visualization purposes, such as for fused PET/CT images.

The uncertainty estimation method presented in this work applies to the ideal situation where the MR acquisitions were performed as planned, without any noticeable motion artifacts in the images and without any detected hardware malfunction or drifts in the system between the acquisition of the reference data and the acquisition for the individual patient. In clinical implementation of the s-CT method, there is a need for rigorous QA measures, both on the scanner and coil level, and also for the individual patient. The design of these tests remains to be determined.

While the second nominal flip angle specified when running the UTE sequences was 60° we have recently discovered that the actual achieved flip angle was less than this due to a limitation in the sequence that resulted in flip angle clipping. Measurements show that no change in contrast occurs beyond a nominal flip angle of 30° and we therefore conclude that this was the actual flip angle of the excitation pulse used in the experiment.

The total acquisition time for the MR sequences used in the present work was approximately 11 min, where 6 min were spent on acquisition of the two double echo UTE sequences with different flip angles and 5 min on the high resolution T2 weighted image. The primary intention with the T2 weighted sequence was to provide information for the

physician when delineating the target volume. Hence, the extra time spent in the scanner was 6 min. In clinical settings, the time aspect is highly important, thus, investigating possible scanning time reduction methods could be of interest. The SPACE sequence provides redundant information in the image set in which both dual echo UTE sequences are included. Therefore, the SPACE sequence could be dropped if not needed for other tasks.

VI. CONCLUSIONS

The EAD of the calculated HU on a voxel level provides an accurate estimation of the MAPD in the MR based s-CT. Only a minor part of the deviations between CT and s-CT are systematic for all densities, except for voxels located in or on the surface of air pockets inside the head. The uncertainty information could make it possible to propagate the uncertainties through a dose calculation or attenuation correction algorithm, to obtain an uncertainty estimation of the clinically relevant measures, absorbed dose and standardized uptake value. Further, for the purpose of s-CT generation,

the non-UTE sequence was found redundant and can be dropped to reduce acquisition time.

ACKNOWLEDGMENT

This work was supported by grants from the Cancer Research Foundation in Northern Sweden and EU Structural Fund Objective 2, Northern Sweden.

APPENDIX: DERIVATION OF EXPECTED ABSOLUTE DEVIATION

Let $\mathbf{Y} = Y$ be a scalar such that $\tilde{\mu}_i = \tilde{\mu}_i$, $\mathbf{m}(\mathbf{x}) = m(\mathbf{x})$ and $\tilde{\Sigma}_i = \tilde{\sigma}_i^2$ are also scalars. The first absolute central moment of a multivariate Gaussian mixture is then given by

$$d(\mathbf{x}) = E(|Y - m(\mathbf{x})| | \mathbf{X} = \mathbf{x}) \\ = \sum_{i=1}^N w_i(\mathbf{x}) \int_{-\infty}^{\infty} |y - m(\mathbf{x})| G(y; \tilde{\mu}_i, \tilde{\sigma}_i^2) dy. \quad (\text{A1})$$

The integral in (A1) can be further simplified

$$\begin{aligned} \int_{-\infty}^{\infty} |y - m(\mathbf{x})| G(y; \tilde{\mu}_i, \tilde{\sigma}_i^2) dy &= \int_{-\infty}^{\infty} |y - m(\mathbf{x})| \frac{1}{\sqrt{2\pi\tilde{\sigma}_i^2}} e^{-\frac{(y-\tilde{\mu}_i)^2}{2\tilde{\sigma}_i^2}} dy = \left\{ \begin{array}{l} v_i = y - \tilde{\mu}_i \\ \kappa_i = m - \tilde{\mu}_i \end{array} \right\} \\ &= \frac{1}{\sqrt{2\pi\tilde{\sigma}_i^2}} \left(\int_{-\infty}^{\kappa_i} (\kappa_i - v_i) e^{-\frac{v_i^2}{2\tilde{\sigma}_i^2}} dv_i + \int_{\kappa_i}^{\infty} (v_i - \kappa_i) e^{-\frac{v_i^2}{2\tilde{\sigma}_i^2}} dv_i \right) \\ &= \kappa_i \operatorname{erf}\left(\frac{\kappa_i}{\sqrt{2\tilde{\sigma}_i^2}}\right) + \sqrt{\frac{2\tilde{\sigma}_i^2}{\pi}} e^{-\frac{\kappa_i^2}{2\tilde{\sigma}_i^2}}. \end{aligned} \quad (\text{A2})$$

Substituting the last line of (A2) into (A1) yields Eq. (15).

^{a)} Author to whom correspondence should be addressed. Electronic mail: adam.johansson@radfys.umu.se

¹M. Karlsson, M. Karlsson, T. Nyholm, C. Amies, and B. Zackrisson, "Dedicated MR in the radiotherapy clinic," *Int. J. Radiat. Oncol. Biol. Phys.* **74**, 644–651 (2009).

²H. Zaidi, "Is MR-guided attenuation correction a viable option for dual-modality PET/MR imaging?," *Radiology* **244**, 639–642 (2007).

³M. Robson, P. Gatehouse, M. Bydder, and G. Bydder, "Magnetic resonance: An introduction to ultrashort TE (UTE) imaging," *J. Comput. Assist. Tomogr.* **27**, 825–846 (2003).

⁴M. Robson and G. Bydder, "Clinical ultrashort echo time imaging of bone and other connective tissues," *NMR Biomed.* **19**, 765–780 (2006).

⁵V. Keereman, R. V. Holen, P. Mollet, and S. Vandenberghe, "The effect of errors in segmented attenuation maps on PET quantification," *Med. Phys.* **38**, 6010–6019 (2011).

⁶J. Jonsson, M. Karlsson, M. Karlsson, and T. Nyholm, "Treatment planning using MRI data: An analysis of the dose calculation accuracy for different treatment regions," *Radiat. Oncol.* **5**, 62 (2010).

⁷L. Chen, R. Price, T. Nguyen, L. Wang, J. Li, L. Qin, M. Ding, E. Palacio, C. Ma, and A. Pollack, "Dosimetric evaluation of MRI-based treatment planning for prostate cancer," *Phys. Med. Biol.* **49**, 5157–5170 (2004).

⁸K. Eilertsen, L. N. Vestad, O. Geier, and A. Skretting, "A simulation of MRI based dose calculations on the basis of radiotherapy planning CT images," *Acta Oncol.* **47**, 1294–1302 (2008).

⁹R. Prabhakar, P. K. Julka, T. Ganesh, A. Munshi, R. C. Joshi, and G. K. Rath, "Feasibility of using MRI alone for 3D radiation treatment planning in brain tumors," *Jpn. J. Clin. Oncol.* **37**, 405–411 (2007).

¹⁰B. H. Kristensen, F. J. Laursen, V. Løgager, P. F. Geertsens, and A. Krarup-Hansen, "Dosimetric and geometric evaluation of an open low-field magnetic resonance simulator for radiotherapy treatment planning of brain tumours," *Radiother. Oncol.* **87**, 100–109 (2008).

¹¹E. Schreiber, J. A. Nye, D. M. Schuster, D. R. Martin, J. Votaw, and T. Fox, "MR-based attenuation correction for hybrid PET-MR brain imaging systems using deformable image registration," *Med. Phys.* **37**, 2101–2109 (2010).

¹²M. Hofmann, F. Steinke, V. Scheel, G. Charpiat, J. Farquhar, P. Aschoff, M. Brady, B. Scholkopf, and B. J. Pichler, "MRI-based attenuation correction for PET/MRI: A novel approach combining pattern recognition and atlas registration," *J. Nucl. Med.* **49**, 1875–1883 (2008).

¹³E. R. Kops and H. Herzog, presented at the Nuclear Science Symposium Conference Record, 2008, NSS '08, IEEE, 2008.

¹⁴C. Catana, A. van der Kouwe, T. Benner, C. Michel, M. Hamm, M. Fenchel, B. Fischl, B. Rosen, M. Schmand, and A. Sorensen, "Toward implementing an MRI-based PET attenuation-correction method for neurologic studies on the MR-PET brain prototype," *J. Nucl. Med.* **51**, 1431–1438 (2010).

¹⁵V. Keereman, Y. Fierens, T. Broux, Y. De Deene, M. Lonneux, and S. Vandenberghe, "MRI-based attenuation correction for PET/MRI using ultrashort echo time sequences," *J. Nucl. Med.* **51**, 812–818 (2010).

¹⁶H. Zaidi, M.-L. Montandon, and D. O. Slosman, "Magnetic resonance imaging-guided attenuation and scatter corrections in three-dimensional brain positron emission tomography," *Med. Phys.* **30**, 937–948 (2003).

¹⁷B. Dogdas, D. W. Shattuck, and R. M. Leahy, "Segmentation of skull and scalp in 3-D human MRI using mathematical morphology," *Hum. Brain Mapp.* **26**, 273–285 (2005).

- ¹⁸G. White and I. Wilson, "Photon, electron, proton and neutron interaction data for body tissues," ICRU Report 46 (1992).
- ¹⁹A. Johansson, M. Karlsson, and T. Nyholm, "CT substitute derived from MRI sequences with ultrashort echo time," *Med. Phys.* **38**, 2708–2714 (2011).
- ²⁰K. V. Mardia, J. T. Kent, and J. Bibby, *Multivariate Analysis* (Academic, London, 1979).
- ²¹H. G. Sung, Ph.D. dissertation, Rice University, 2004.
- ²²J. P. Mugler, S. Bao, R. V. Mulkern, C. R. Guttmann, R. L. Robertson, F. A. Jolesz, and J. R. Brookeman, "Optimized single-slab three-dimensional spin-echo MR imaging of the brain," *Radiology* **216**, 891–899 (2000).
- ²³J. Park, J. P. Mugler, W. Horger, and B. Kiefer, "Optimized T1-weighted contrast for single-slab 3D turbo spin-echo imaging with long echo trains: Application to whole-brain imaging," *Magn. Reson. Med.* **58**, 982–992 (2007).